

# Supplementary discussions

## Table of Contents

1. Structure of carbonaceous materials and characterization thereof .....	2
1.1 Graphite .....	2
1.2 Soft carbon .....	2
1.3. Hard carbon .....	5
2. Porosity characterization .....	7
2.1 Gas sorption .....	7
2.2 Small angle x-ray scattering (SAXS) .....	9
3. Comparison of SIB performance of carbonaceous materials .....	10
4. Comparison of SIB performance of organic electrode materials .....	12
5. References.....	16

## 1. Structure of carbonaceous materials and characterization thereof

Carbonaceous anode materials proposed for SIBs include graphitic and non-graphitic carbons, the latter of which are further classified into soft and hard carbon as distinguished by their long- and short-range order, which is typically assessed by the width and position of the (002) stacking periodicity. Graphene and related carbon types, either as isolated monolayers or few-layer stacks, may be considered as a separate class to the soft and hard carbons, since they have periodicity in the lateral direction but tend to be highly disordered in the stacking direction, with an interlayer spacing between that of soft and hard carbon. In terms of sodium storage, a general trend from the lowest to highest specific capacity is graphite, soft carbon and then hard carbon.

### 1.1 Graphite

Natural and synthetic graphite comprises predominantly sp<sup>2</sup> carbons in hexagonal two-dimensional arrays (i.e. graphene) that stack together through van der Waals interaction at an interlayer separation of 3.3 Å. Stacking is either in an ABAB arrangement (hexagonal 2H) or an ABCABC order (rhombohedral 3R), both of which are commonly described by the relative fractions of 2H and 3R<sup>1</sup>. Stacking or turbostratic disorder can occur if the graphene layers shift or rotate away from their idealized stacking arrangement. The layering in this crystalline material permits intercalation of Li<sup>+</sup> to a theoretical stoichiometry of LiC<sub>6</sub> with a concomitant transformation to AAAA stacking<sup>2-6</sup>, and is electrochemically characterized in the galvanic profile by a plateau at the low voltage region. Although graphite anode has long, cyclable capacity for lithium storage close to the theoretical 372 mAh g<sup>-1</sup>, its sodiation/desodiation capacity is very low at 40 mAh g<sup>-1</sup> and was initially attributed to the interlayer spacing being too small to accommodate the larger Na ion.

### 1.2 Soft carbon

Soft carbons are typically derived from (poly)aromatic precursors with low oxygen contents, such as pitch or tar from the refinement of petroleum and coal. They are typically heat-treated from 700 to 900 °C, well below the graphitization temperature of 2500 °C<sup>7</sup>. However, they are considered to be graphitizable, but due to the lower heat treatment temperature, the graphene layers have defects in the form of dislocations, curvature and tilt, as well as other types of defects such as non-carbon elements and 5-member carbon rings at the layer edges (described further below)<sup>8</sup>. These defects lead to some turbostratic disorder that weakens layer-to-layer interactions, resulting in enlarged interlayer spacing to 3.7–4.0 Å<sup>9</sup>, nanometer-scale porosity from stacking faults, and mechanical softness as indicated by their appellation “soft carbon”<sup>10-12</sup>. These defects have been implicated in the sodium storage mechanism, and their density and characteristics are dependent on their synthesis parameters, as systematically investigated by, for example, Tan et al.<sup>13</sup>. In this work, soft carbon was prepared in the temperature range 800–2800 °C (notated in Figure S1 a-f as SC-X where SC stands for soft carbon and X is the heating temperature). Based on high resolution TEM analysis (Figure S1a-d), it can be visualized that the graphene layers have the typical turbostratic structure from 800 to 1400 °C, though the layers themselves can be curved but have some degree of alignment. Alignment into stacks of parallel sheets commences at 2000 °C, and then finally graphitizing at 2800 °C to have a regular interlayer separation. As corroborated by XRD (Figure S1e), increasing the temperature from 800 to 2800 °C narrows the interlayer spacing progressively from 3.56 to 3.37 Å. Although the final interlayer spacing is identical to that of natural graphite, significant number of disordered domains is retained even when heated to 2800 °C; complete graphitization requires long heating duration possibly together with higher temperature or applied pressure. These trends are corroborated in their Raman spectra which, as shown in Figure S1f, have the D band even in the pristine state, contrasting that of graphite in the previous section. Upon increasing the heat treatment temperature towards 2800 °C, the intensity of the D band decreases relative to the G band intensity. The authors also stated

that the emergence of the 2D band at around  $2700\text{ cm}^{-1}$  at  $2000\text{ }^{\circ}\text{C}$  and above is an indication of an increasing number of graphene layers stacked together, although this interpretation is debatable because this band is also present in single layer graphene<sup>14</sup>. One Raman-based metric for quantifying defect is the ratio of the D-band intensity to the G-band intensity, typically notated in the literature as  $I_D/I_G$ . With increasing heating temperature, this ratio decreases as confirmation of the progressive graphitization and loss of defects in the soft carbon. At this point, it should be noted here that this work primarily studied the use of soft carbon as anode in potassium ion batteries.

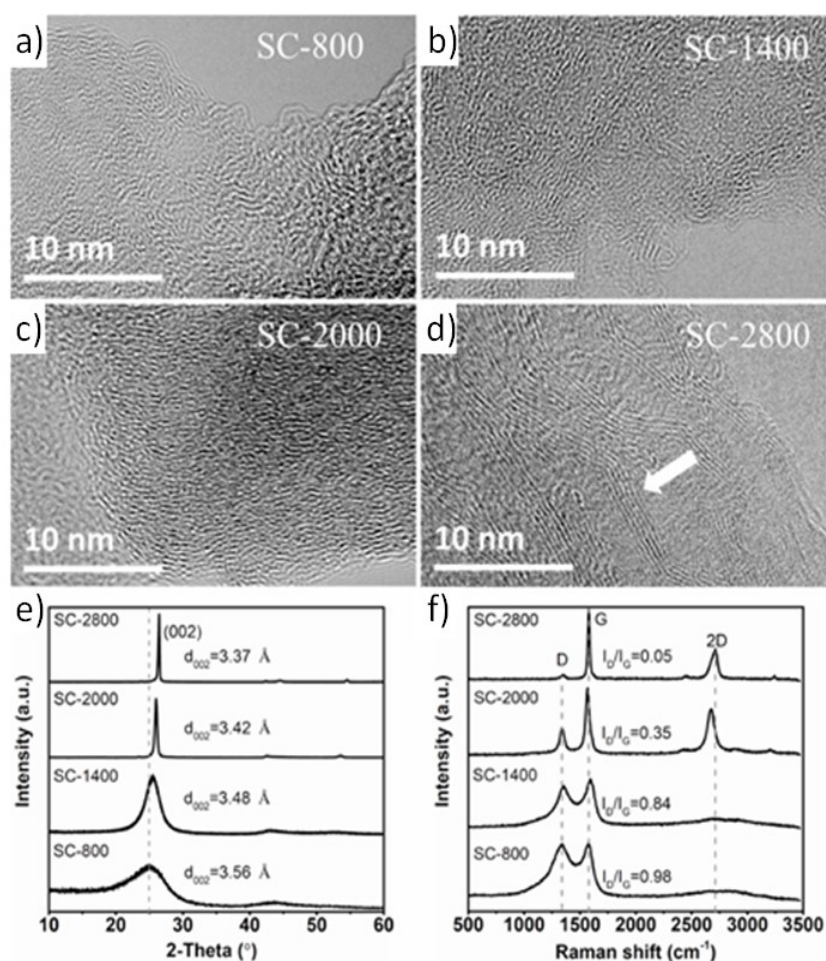


Figure S1 TEM images of a) SC-800, b) SC-1400, c) SC-2000, and d) SC-2800; e) XRD patterns and f) Raman spectra for SC-800, SC-1400, SC-2000 and SC-2800. Adapted from reference <sup>13</sup> with permission from El Sevier.

In addition to the characterization techniques above, soft carbon has been investigated by neutron diffraction as analyzed by pair distribution function (PDF), which is an analytical method to yield real space structure obtained by performing Fourier transform on the total scattering data, thus giving a histogram of atomic pair distances<sup>15</sup>. As this method analyzes total scattering data, it allows analysis of local structure making it particularly useful for carbonaceous samples. This method was applied by Jian et al. to compare the structure of soft and hard carbon<sup>16, 17, 16</sup> using graphite as the reference, as shown in Figure S2a-b. Within the Ångstrom range, it is immediately obvious that the intensities of the peaks for soft carbon (SC) are much smaller than that of graphite, especially at higher r-values. Since peak integral is proportional to the number of atom pairs at a specific separation distance, the PDF results suggest soft carbon to have more in-plane defects such as curvature of the individual graphene layers. Correspondingly, while graphite exhibits peaks in the PDF profile over a longer range

to above 20 Å, the profile for soft carbon is indiscernible above 10 Å indicating lack of long-range order, likely in both in-plane and through-plane direction (which cannot be distinguished by PDF). X-ray PDF was also employed by Ou et al. to investigate structural ordering of soft carbon as a function of synthesis temperature, ranging from 900 to 2900 °C, as shown in Figure S2c (notated as SC-X where X is the synthesis temperature)<sup>18</sup>. Within the immediate bonding environment covering nearest or next nearest neighbors up to 3 Å, the PDF profiles are quite similar for all soft carbon samples, indicating that most carbons are bonded in an identical fashion with a negligible number of vacancies, hetero-atoms, or similar kinds of defects. At the medium range of 3–10 Å, intensity difference is evident; at long range up to around 80 Å, peaks are only evident for the high-temperature samples, while peaks appear broad or smeared out for the low temperature sample. Combined, these results suggest that crystallographic defects in soft carbons are the curvature of the graphene layers and stacking irregularities. Of the latter, through fitting of the PDF profiles, the displacement factor in the through-plane direction,  $U_{33}$ , can be extracted and provides a metric for stacking disorder (i.e. higher  $U_{33}$  indicates increased stacking disorder). As plotted in Figure S2d,  $U_{33}$  and hence disorder remains similar until an abrupt increase for SC-1800, presumably a transitional sample, and then drastically decreased for samples prepared above 2100 °C.

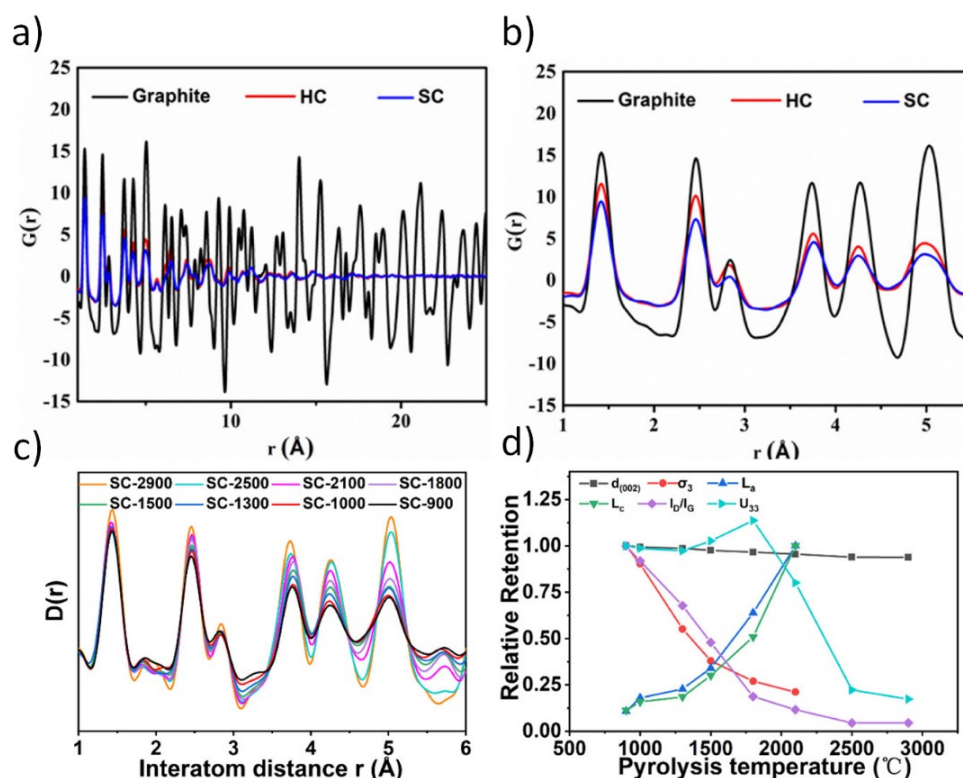


Figure S2 a) PDF analysis of neutron total scattering of soft carbon (SC), hard carbon (HC), and graphite of up to 25 Å, with a magnification of the short-range profile shown in panel b. c) PDF profiles from 1 to 6 Å of SCs prepared at different temperature; d) plots of the normalized structural parameters for the SC samples prepared at different temperature. Panels a and b was adapted from reference<sup>16</sup>, and panels c and d were adapted from reference<sup>18</sup>, with permission from the American Chemical Society.

Overall, these results are consistent with the trends in Raman spectroscopy and other characterization methods discussed above, where increasing the heating temperature leads to increased short- and long-range order, approaching characteristics similar to those of graphite when heated close to the graphitization temperature at or above 2000 °C. In the publications cited above, the consensus is that ion storage capacity of soft carbon is inversely proportional to the heating temperature, maximizing at 300 mAh  $g^{-1}$  when prepared at 900 °C, and then decreasing upon heating at higher temperature

(reiterating that this work was for potassium storage, though the findings here can also be translated for the study of sodium storage). At the optimum temperature, long range order is rather weak, thus implicating several structural features to be responsible for sodium storage, including widened interlayer separation, stacking faults, curvature of the graphene layers/stacks and the resultant misalignment, as well as other non-graphitic microstructural properties. This implication is also reflected in the profile of the galvanic curves, which are sloped during both sodiation and desodiation without any plateau in the low voltage region from the second cycle onward, in contrast to graphite (and hard carbon as will be seen in the next section). It should be noted that, since much of its reversible capacity originates from voltage above where sodium plating occurs, soft carbon may have reduced hazard associated with dendrite formation and high reactivity. Another observation is that the Coulombic efficiency in the first cycle is as low as 67.6%, coupled with a quasi-plateau in the galvanic profile during sodiation that has been assigned to irreversible intercalation or defect binding. By extension, other types of defects and structural features in soft carbon would be responsible for reversible sodium storage.

### 1.3. Hard carbon

Hard carbons are derived from precursors that have significant amount of non-carbon elements, and have molecular features that prevent graphitization. Cellulose is one example of a polymeric precursor that is constituted of hydrogen and oxygen (in addition to carbon) and has a large number of cross-links, all of which disrupt ordering and densification of the carbon layered structure<sup>19, 20</sup>. Volatilization of the non-carbon elements, which occurs typically in the range of 300–500 °C, leads to gas evolution that confers significant microporosity (pore diameter <2 nm as per IUPAC definition) to the final material. Hard carbons are thus not graphitizable, and have been described with a “house of cards” analogy where crystalline domains are dispersed within amorphous regions<sup>21, 22</sup>. Hence, compared to soft carbon, hard carbon smaller crystalline domains and has higher porosity from both stacking faults as well as inherent porosity from precursor volatilization. When prepared at above 1000 °C, hard carbon exhibits sodium storage capacity larger than both graphite and soft carbon, and much research has been dedicated to correlating each structural feature to the ion storage mechanism. Ion intercalation is thought to occur within the nanocrystalline domains where some stacking order exists in a process identical to graphite as described above, while the small number of heteroatoms such as oxygen can bind to the sodium, the so-called defect-binding. From the “house of card” analogy, sodium can also be stored on the surfaces the random stacks of graphene by adsorption, and in the microporosity and in the pores generated by stacking faults by pore filling<sup>21-23</sup>. The prevalence of each of these structural features, and in turn their chemical properties and their dominant charge storage mechanism, is dependent on the heat treatment parameters, though there is general agreement in the literature that battery performance is optimized when the hard carbon is prepared in the range of 1300–1600 °C. The ion storage mechanism of hard carbon depends on the ions stored. This ion dependency was recently studied by Alvin et al.<sup>24</sup>, who compared Li, Na and K storage in hard carbon prepared at 1300 °C (denoted as HC-1300). Their galvanic profiles are displayed in Figure S3a-c. For lithium and potassium, the galvanic profiles have slopes of different gradients yielding relatively lower capacities of 220 and 246 mAh g<sup>-1</sup>, respectively. For sodium, there is a flat galvanic plateau at a voltage of ≈0.1 V, which encompasses the majority of the total discharge capacity of 287 mAh g<sup>-1</sup>. This flat plateau indicates the energetics of the storage sites and mechanism are similar for sodium. In contrast, the sloping galvanic profiles for lithium and potassium suggest the ion storage site and mechanism have a broad range of energies.

Similar to soft carbon, the structural characteristics of hard carbon is dependent on their synthesis parameters and can be characterized by spectroscopy, diffractometry and electron microscopy. Figure

S3d shows the Raman spectra of hard carbon prepared at 600 to 2500 °C as indicated by the numeral in the sample labels.<sup>47</sup> Here, the D band has substantial intensity relative to the G band, indicating hard carbon is composed of smaller in-plane domains of graphitic structure than soft carbon and graphite. Elevating the heat treatment temperature sharpens both bands and increases the  $I_G/I_D$  ratio corresponding to defect removal. When prepared at 2500 °C, the highest temperature employed in this study, the  $I_G/I_D$  ratio of hard carbon maximized at 9.19. This implies a graphite-like structure (as consistent with XRD and TEM results; see below) although a minute amount of defect remains as evident by the small but discernible D band. Another band at  $\approx 2700\text{ cm}^{-1}$  appears as the pyrolysis temperature increases to 1500 °C, of which the authors of this study attribute to the elimination of dangling bonds and formation of curved graphitic layers<sup>25</sup>. However, this interpretation is imprecise, given that this band denoted in the graphene literature as the 2D band is always observed in both defect-free and defected graphene<sup>14</sup>. An alternative interpretation may be that, from 1500 °C onward, the hard carbon begins to develop a graphene-like structure.

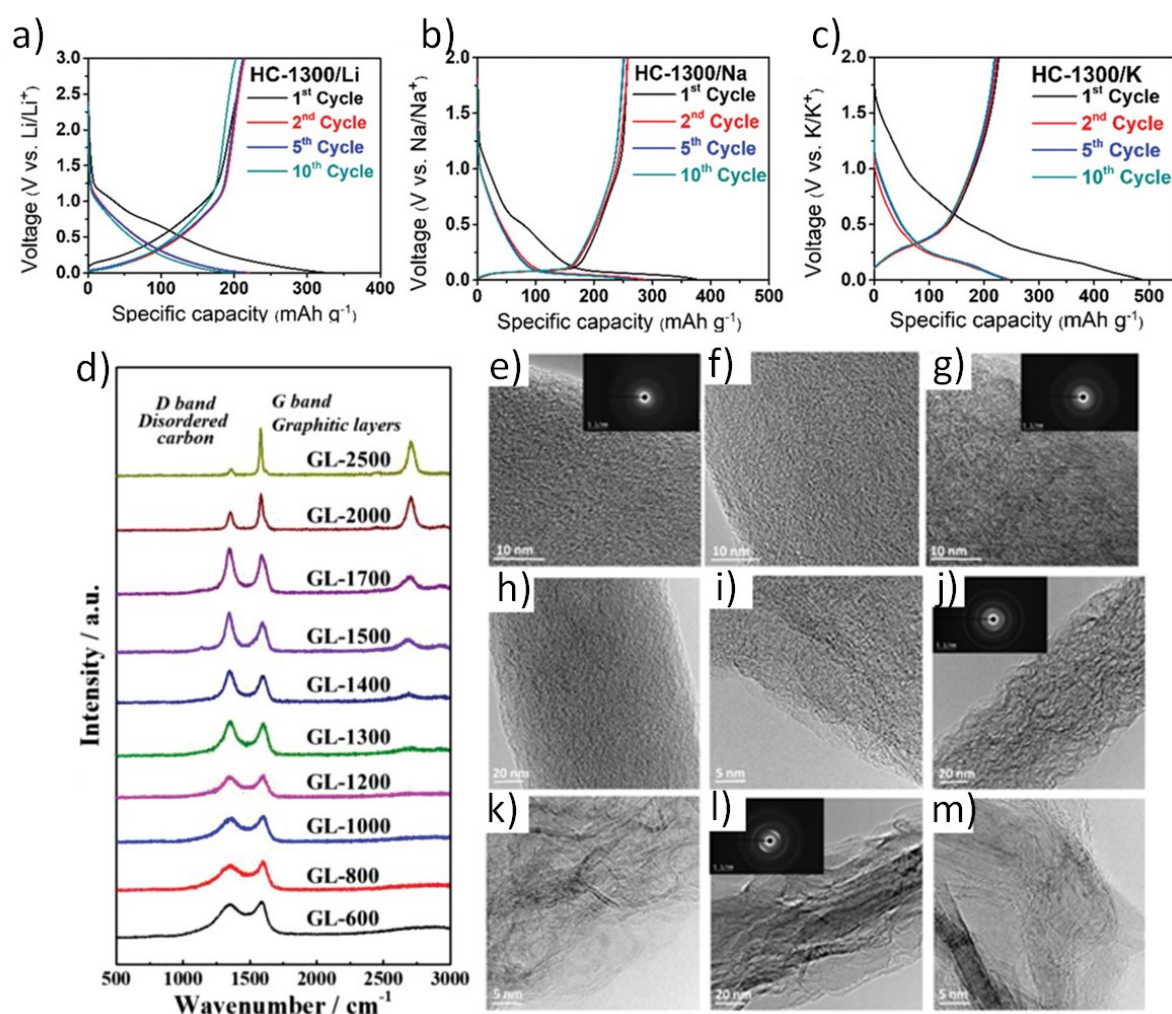


Figure S3 Galvanic discharge–charge profiles at current of 50 mA g<sup>-1</sup> of the initial 10 cycles of hard carbon for storing lithium (a), sodium (b) and potassium (c). d) Raman spectra of GL-X samples synthesized at various temperature; TEM images of fibrous hard carbon prepared at e) 650 °C, f) 950 °C, g) 1250 °C, h–i) 1550 °C, j–k) 2200 °C, and l–m) 2800 °C. Panels a–c are adapted from reference <sup>26</sup>, panel d from reference <sup>27</sup>, and panels e–m adapted from reference <sup>24</sup> with permission from John Wiley & Sons.

These Raman results have been corroborated by a separate study by Zhang et al. who, to track changes in crystallinity, performed TEM analyses of hard carbon, likewise prepared at different temperatures

but with an electrospinning method to yield fibrous hard carbon<sup>24</sup>. As seen in Figure S3e-m, the hard carbon samples did not exhibit ordering graphitic layers when prepared below 1550 °C but begin to be observable when synthesized above 2200 °C as seen in Figure S3j-m. Finally, when prepared at 2200 and 2800 °C, stacks and layers are formed, presumably as defects (e.g. layer curvature) are reduced to allow the graphene stacks to align and densify. However, even at above 2200 °C, these TEM images show that the continued presence of some curvature and stacking disorder. Combined, these literature results consistently show defect reduction and crystallinity increase are accompanied by higher heat treatment temperature. The optimum temperature range of 1300–1600 °C for maximizing specific capacity, however, would suggest that sodium storage takes place at structural defects, including sodium pore filling of micropores generated from stacking faults (Figure S4a) and those produced by precursor volatilization.

## 2. Porosity characterization

Since porosity is implicated as a sodium storage site, its characterization is an essential aspect of hard carbon research. The two main methods are often used for porosity characterization: gas sorption and small angle x-ray scattering (SAXS).

### 2.1 Gas sorption

Gas sorption is typically employed in accordance with the Langmuir or Brunauer–Emmett–Teller (BET) theory for monolayer and multilayer gas sorption, respectively, for quantifying the specific surface area. Porosity can be modelled and quantified using the 2D non-local density functional theory (NLDFT) heterogeneous surface model for carbonaceous materials, assuming slit-type pores between infinitely large graphitic surfaces<sup>28, 29</sup>. Gas sorption as a characterization method specifically probes pores that are accessible to the gas molecules i.e. “open pores”. The opposite is the “closed pores” that are embedded within the carbon and thus inaccessible to the gas sorbent. When referring to porosity, IUPAC provides the following standardized terminologies: micropores for pores of diameter <2 nm and mesopores for 2–50 nm. In selecting the gas used for the sorption analysis, nitrogen is most typically used although the texture properties calculated from N<sub>2</sub> adsorption has a large measurement uncertainty for materials with low surface area, since most if not all instruments quantify the adsorbed gas by measuring pressure change. Hence, nitrogen as sorbent is unsuitable for hard carbons prepared at high temperature, which may have a surface area below 10 m<sup>2</sup> g<sup>-1</sup> and close to the detection limit for N<sub>2</sub> sorption. Krypton sorption at 77 K is the conventional method for analyzing materials with smaller surface area, since their much lower vapor pressure induces a large pressure change even when small amount of this gas is adsorbed, and can thus be measured with great accuracy. However, it is an expensive gas, and the larger atomic size of krypton was found to yield smaller-than-expected surface area, which may be due to limited access of this gas into the smaller micropores (<7 Å) of hard carbon. Hence, to best identify the gas most suitable for rigorous characterization of the hard carbons, Ghimbeu et al. investigated how surface area and porosity results from gas sorption analysis are dependent on the type of gas used<sup>30</sup>. In this work, they employed on N<sub>2</sub>, Ar, CO<sub>2</sub>, O<sub>2</sub> and H<sub>2</sub>, the key data of which are summarized in Table S1. Adsorption/desorption isotherms using these gases and the corresponding pore size distribution are shown in Figure S4b and c, respectively.

Adsorbate	Molecular size nm	Quadrupole moment	Polarizability ×10 <sup>-25</sup> cm <sup>3</sup>	SSA m <sup>2</sup> g <sup>-1</sup>	V <sub>t</sub> cm <sup>3</sup> g <sup>-1</sup>	L <sub>0</sub> nm
-----------	-------------------	-------------------	---	------------------------------------	--	-------------------

$\times 10^{40} \text{ cm}^2$

N <sub>2</sub>	0.364	-4.91	17.4	19	0.012	1.87
Ar	0.340	0.00	16.4	12	0.007	1.45
CO <sub>2</sub>	0.330	-13.71	29.1	91	0.024	0.94
O <sub>2</sub>	0.346	-1.33	15.8	279	0.112	1.22
H <sub>2</sub>	0.289	2.2	8.1	113	—	0.52

Table S1 Properties of the sorption gases and a summary of the textural properties of the hard carbon prepared at 1300 °C as dependent on the sorption gas used for collecting its isotherms; here, SSA refers to the specific surface area as modelled by BET theory,  $V_t$  the total pore volume, and  $L_0$  the average pore size. Data obtained from reference <sup>31</sup>.

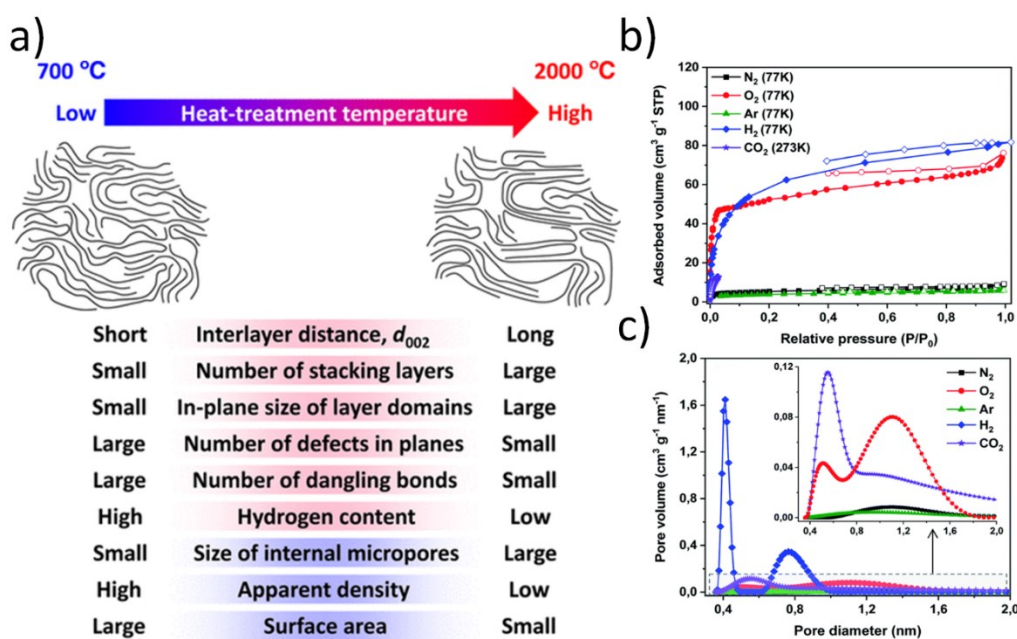


Figure S4 a) Schematic illustration summarizing the differences in hard carbon structure when prepared at 700 and 2000 °C. b) Comparison of the adsorption–desorption isotherms using different gases as sorbent on hard carbon prepared at 1300 °C. c) 2D-NLDFT pore size distribution histograms based on the isotherm of different gas sorbents. Panel a adapted from reference <sup>25</sup> with permission from the American Chemical Society, and panels b-c is adapted from reference <sup>31</sup> with permission from Royal Society of Chemistry.

H<sub>2</sub> and O<sub>2</sub> were found to yield the greatest specific surface area and total pore volume, followed by CO<sub>2</sub>, and then N<sub>2</sub> and Ar. While there is a correlation between the gas atomic/molecular size and the pores accessible, other factors such as the gas' diffusivity, quadrupole moment and polarizability also play a part. This may be the case if the substrate has polar functional groups on the surface, leading to possible intermolecular interactions with the sorbent gas owing to their polarizability and quadrupole moment, and thus altering the gas sorption dynamics. Here, it should be noted that, for the BET model which is itself an extension of the Langmuir adsorption model, one of the underlying assumptions is that the substrate surface is homogeneous and terminated by only one type of

functional group; whether the key assumptions underpinning these sorption models are still justified remains to be ascertained. As another complication, in the case of linear sorbent molecule, the quadrupole moment seems to affect the orientation of adsorption (i.e. lying parallel or perpendicular to the surface) leading to differences in total gas adsorbed and, in turn, the surface area and porosity calculated. Otherwise, on the balance of safety and accessibility, CO<sub>2</sub> sorption at 273 K is one of the more suitable probe gases owing to its small kinetic diameter of 330 pm (c.f. 360 pm for Kr and 364 pm for N<sub>2</sub>). Measurement at this high temperature is also thought to provide better access to the narrowest micropores<sup>30</sup>. Based on these considerations, Kim et al. attempted to characterize all of the open pores, especially the micropores, by performing the gas sorption analysis with CO<sub>2</sub> at an even higher temperature of 293 K so as to improve gas diffusivity and penetration. However, this higher temperature analysis may not be appropriate, since the adsorptivity of the gas is reduced due to the higher molecular mobility with increased temperature<sup>32</sup>.

## 2.2 Small angle x-ray scattering (SAXS)

SAXS is similar to x-ray diffraction, but records x-ray scattered at very small angle corresponding to length scale of typically 1–100 nm. Regardless of sample crystallinity, the intensity of the scattered x-ray is proportional to the autocorrelation of every pair of x-ray scatterer (i.e., electrons in atoms), such that a plot of the intensity as a function of distance (or the inverse,  $q$ , in units of nm<sup>-1</sup> or Å<sup>-1</sup>) gives a histogram-like graph showing which structural features (or strictly speaking, the sizes of the structure features) are the most prevalent. Due to the penetration depth of x-ray, all structural features inclusive of open and closed porosity can be probed, making SAXS complementary to the gas sorption technique, as well as complementing X-ray diffraction to provide structural insights at Ångstrom to nanometer scale. Moreover, SAXS is particularly suitable for analyzing cycled electrodes, as the x-ray can penetrate through the SEI that would otherwise block gas diffusion preventing gas sorption analyses<sup>25</sup>.

Using both gas sorption and SAXS, together with other corroborative methods, structural and morphological trends could be identified in hard carbons prepared at different temperature. Increasing from 700 to 2000 °C, BET surface area decreases, and is accompanied by a reduction of open pores either in terms of the number of open pores or of total open pore volume. This is accompanied by a concomitant increase in the size and volume of closed pores as detected by SAXS and TEM<sup>25</sup>.

### 3. Comparison of SIB performance of carbonaceous materials

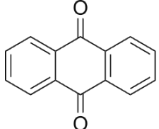
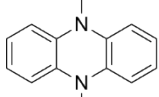
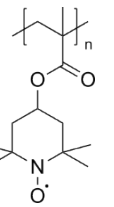
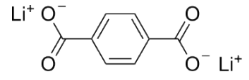
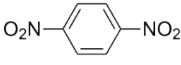
Table S2 SIB performance of selected carbonaceous electrode compounds reviewed here

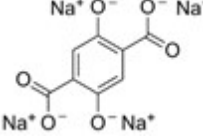
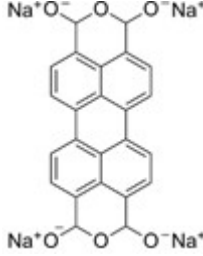
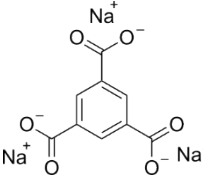
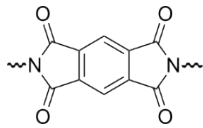
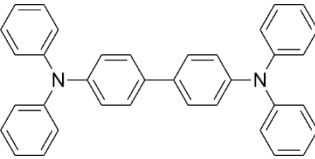
Carbon type	Special condition	Final heat treatment(°C)	Voltage window (V)	Current density (mA g <sup>-1</sup> )	Capacity (mAh g <sup>-1</sup> )	Initial coulombic efficient	Durability capacity (current density) [Cycle number]	Year paper published	Reference
Graphite	Expanded graphite	—	0-2	20	284	49.45	180 (100mA g <sup>-1</sup> ) [2000]	2014	33
Graphite	Graphite in 1 M NaCF <sub>3</sub> SO <sub>3</sub> with TGM	—	0.01-2	100	110	—	110 (0.2 Ag <sup>-1</sup> ) [6000]	2015	34
Graphite	Natural graphite in NaPF <sub>6</sub> in DEGDME	—	0.001-2.5	100	150	—	125 (500 mA g <sup>-1</sup> ) [2500]	2014	35
Graphite	Graphite in tetraethylene glycol dimethyl ether	—	0.1–2.0	50	130	—	140 (0.1A g <sup>-1</sup> ) [100]	2019	36
Graphite	Graphite in mono-glymes electrolyte	—	0.01-2.5	11	97.6	—	—	2018	37
Graphite	Graphite in di-glymes electrolyte	—	0.01-2.5	11	109.8	—	—	2018	37
Graphite	Graphite in tri-glymes electrolyte	—	0.01-2.5	11	65	—	—	2018	37
Graphite	Graphite in tetra-glyme electrolyte	—	0.01-2.5	11	102	—	—	2018	37
Graphite	Graphite in Penta-glyme electrolyte	—	0.01-2.5	11	20	—	—	2018	37
Soft carbon	Phosphorus-doped soft carbon	900	0.001-2	100	251	—	201 (100 mA g <sup>-1</sup> ) [200]	2017	38
Soft carbon	PTCDA(C <sub>24</sub> H <sub>8</sub> O <sub>6</sub> )	700	0.01–2	20	233	62.6	114 (1000 mA g <sup>-1</sup> ) [300]	2015	39
Soft carbon	Powdery mesophase pitch and nano-CaCO <sub>3</sub>	800	0.01–3	30	331	—	103 (500 mA g <sup>-1</sup> ) [3000]	2017	17
Soft carbon	The coal tar pitch (CTP) with H <sub>3</sub> PO <sub>4</sub>	900	0.001-2	100	251	—	201 (100mA g <sup>-1</sup> ) [200]	2016	38
Soft carbon	PTCDA	900	0.01-2	20	195	—	—	2017	16
Soft carbon	Microporous soft carbon nanosheets	800	0.01–3	20	232.2	—	128.7 (800mA g <sup>-1</sup> ) [3500]	2017	40

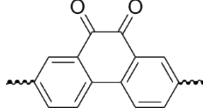
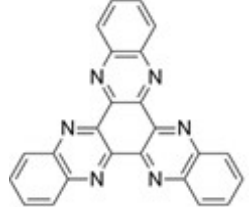
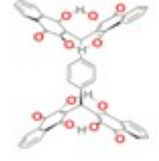
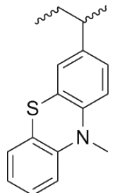
Hard carbon	Lignin	1300	0.005-2.5	50	260.55	69	141 (0.3 A g <sup>-1</sup> ) [700]	2019	<sup>41</sup>
Hard carbon	Peat moss leaves	1100	0.001-2.8	50	298	57.5	255 (100mA g <sup>-1</sup> ) [200]	2013	<sup>42</sup>
Hard carbon	Sucrose with H <sub>3</sub> PO <sub>4</sub>	1100	0.01-2	20	245	80.5	327 (20 mA g <sup>-1</sup> ) [200]	2017	<sup>15</sup>
Hard carbon	Ginkgo leaf	1300	0.001-3	30	416.2	—	250 (50 mA g <sup>-1</sup> ) [200]	2019	<sup>27</sup>
Hard carbon	Sucrose	1300	0.002-2	25	324	—	—	2020	<sup>25</sup>
Hard carbon	Microcrystalline cellulose	1300	0.005-1.5	20	300	79	280 (20mA g <sup>-1</sup> ) [80]	2021	<sup>32</sup>
Hard carbon	Kapok fibers	1400	0-2	30	290	80	250 (30mA g <sup>-1</sup> ) [200]	2020	<sup>43</sup>
Hard carbon	Kapok fibers	1500	0.005–2.5	30	293	85	—	2020	<sup>44</sup>
Hard carbon	MgO template	1500	0.002–2	25	478	88	450 (25mA g <sup>-1</sup> ) [35]	2021	<sup>45</sup>

## 4. Comparison of SIB performance of organic electrode materials

Table S3 SIB performance of selected organic electrode compounds reviewed here

Molecular structure and theoretical capacity	1 <sup>st</sup> cycle capacity in mAh g <sup>-1</sup> ; CE in parentheses	Long term capacity retention in mAh g <sup>-1</sup> ; CE in parentheses	High rate capacity in mAh g <sup>-1</sup>	Redox potential and other battery cell parameters
 Anthraquinone <sup>46</sup>	214 at 0.2C (97%)	190 at 50 <sup>th</sup> cycle, 0.2C (80%)	143 at 2C (n/a)	1.7 V vs Na, 4 M NaCF <sub>3</sub> SO <sub>3</sub> in TEGDME Electrode prepared with the mesoporous carbon CMK-3
 Dimethylphenazine <sup>47</sup>	250 at 0.2C (83%)	200 at 50 <sup>th</sup> cycle, 0.2C (99%)	49 at 8C (n/a) for one-electron reaction	3.0 and 3.7 V vs Li, 1 M LiPF <sub>6</sub> in EC/DMC/EMC (1:1:1 v/v/v); electrode prepared with non-oxidized graphene flakes and cellulose nanofibers
 Poly(4-methacryloyloxy-TEMPO) <sup>48</sup>	120 at 1C (83%)	105 at 25 <sup>th</sup> cycle, 1C (99+%)	97 at 2C (99+%)	3.6 V vs Li, 1 M LiPF <sub>6</sub> in EC/DMC (1:1 v/v) Cross-linked polymer
 Dilithium terephthalate <sup>49</sup>	173 at 1C (n/a)	110 at 50 <sup>th</sup> cycle, 1C (n/a)	n/a	1.1 V vs Li, 1M LiTFSI in TEGDME
 Para-dinitrobenzene <sup>50</sup>	573 at 50 mA g <sup>-1</sup> (94%)	289 at 50 <sup>th</sup> cycle, 50 mA g <sup>-1</sup> (99%+)	200 at 200 mA g <sup>-1</sup> (n/a)	2.1 V and 1.6 V vs Na, 1 M NaTFSI in DOL/DME (1:1 v/v) Mixed with microporous carbon nanospheres (diameter 40 nm)

 <p>Tetrasodium 2,5-dihydroxyterephthalate<sup>51</sup></p>	183 at 0.1C (90%)	154 at 100 <sup>th</sup> cycle, 0.1C (99+%)	75 at 5C (n/a)	0.3 V or 2.3 V vs Na, 1 M NaClO <sub>4</sub> in EC/DMC (1:1 v/v)
 <p>Tetrasodium perylene 3,4,9,10-tetracarboxylic dianhydride<sup>52</sup></p>	620.5 at 25 mA g <sup>-1</sup> (61%)	251 at 140 <sup>th</sup> cycle, 25 mA g <sup>-1</sup> (99+%)	68 at 2000 mA g <sup>-1</sup> (99+%)	1.0 V vs Na, 1 M NaPF <sub>6</sub> in EC/DMC (1:1 w/w)
 <p>Trisodium 1,3,5-benzenetricarboxylate<sup>53</sup></p>	250 at 0.2C (44.8)	200 at 100 <sup>th</sup> cycle, 0.2C (99+%)	100 at 10C (n/a)	0.5 V vs Na, 1 M NaBF <sub>4</sub> in tetraglyme
 <p>Pyromellitic diimide polymer<sup>54</sup></p>	149 at 0.1C (81)	138 at 400 <sup>th</sup> cycle, 0.1C (99+%)	96.4 at 8C (99+%)	2.1 V vs Na, 1 M EC/DMC (1:1 w/w)
 <p>N,N,N',N'-tetraphenyl-1,1'-biphenyl-4,4'-diamine<sup>55</sup></p>	77.4 at 50 mA g <sup>-1</sup> (n/a)	47 at 450 <sup>th</sup> cycle, 50 mA g <sup>-1</sup> (n/a)	52 at 1000 mA g <sup>-1</sup> (n/a)	3.7 V vs Li, 3 M LiPF <sub>6</sub> in DMC/FEC (9:1 v/v)

 Phenanthrenequinone polymer <sup>56</sup>	130 at 0.5C (99+%), 10 <sup>th</sup> cycle	146 at 400 <sup>th</sup> cycle, 0.5C (96%)	61 at 5C (95%)	2.3 V vs Mg, 0.6 M Mg(TFSI)2-2MgCl <sub>2</sub> in DME
 Triquinoxalinylene <sup>57</sup>	5 <sup>7</sup> 41 at 100 mA g <sup>-1</sup> (n/a)	135 at 100 <sup>th</sup> cycle, 350 ma g <sup>-1</sup> (n/a)	n/a	1.77, 1.36, 0.95, 0.59, 0.39, 0.19 V vs Na, 1 M NaPF <sub>6</sub> in diglyme; electrode prepared with sodiated Nafion for long term stability test
 Tetrakislawsonone <sup>58</sup>	230 at 50 mA g <sup>-1</sup> (85%)	90 at 325 <sup>th</sup> cycle, 50 mA g <sup>-1</sup> (99+%)	40 at 1000 mA g <sup>-1</sup> (99+%)	1.8 and 2.4 V vs Na, 1 M NaClO <sub>4</sub> in TEGDME
 Poly(vinylphenothiazine) <sup>59</sup>	58 at 1C (50%)	50 at 1000 <sup>th</sup> cycle, 1C (99+%)	33 at 10C (99+%)	3.7 V vs Li, 1 M LiPF <sub>6</sub> in EC/DEC (1:1 v/v)

n/a: data not available  
 CE: Coulombic efficiency  
 EMC: ethyl methyl carbonate

DMC: dimethyl carbonate  
 EC: ethylene carbonate  
 DMC: dimethyl carbonate

TFSI anion: bis(trifluoromethanesulfonyl)imide  
 DOL: 1,3-dioxolane  
 DME: 1,2-dimethoxyethane

TEGDME: tetraethylene glycol dimethyl ether  
 FEC: fluoroethylene carbonate  
 DME: dimethoxyethane

## 5. References

1. D. Saurel, J. Segalini, M. Jauregui, A. Pendashteh, B. Daffos, P. Simon and M. Casas-Cabanas, *Energy Storage Mater.*, 2019, **21**, 162-173.
2. M. Winter, J. O. Besenhard, M. E. Spahr and P. Novak, *Adv. Mater.*, 1998, **10**, 725-763.
3. A. Metrot, D. Guerard, D. Billaud and A. Herold, *Synth. Met.*, 1980, **1**, 363-369.
4. P. Ge and M. Foulletier, *Solid State Ion.*, 1988, **28**, 1172-1175.
5. N. Adhoum, J. Bouteillon, D. Dumas and J. C. Poignet, *Electrochim. Acta*, 2006, **51**, 5402-5406.
6. H. Moriwake, A. Kuwabara, C. A. Fisher and Y. Ikuhara, *Rsc Advances*, 2017, **7**, 36550-36554.
7. H. Azuma, H. Imoto, S. i. Yamada and K. Sekai, *J. Power Sources*, 1999, **81**, 1-7.
8. D. Saurel, B. Orayech, B. Xiao, D. Carriazo, X. Li and T. Rojo, *Adv. Energy. Mater.*, 2018, **8**, 1703268.
9. W. Zhang, F. Zhang, F. Ming and H. N. Alshareef, *EnergyChem*, 2019, **1**, 100012.
10. R. E. Franklin, *Acta Crystallogr.*, 1951, **4**, 253-261.
11. F. Cowlard and J. Lewis, *JMats*, 1967, **2**, 507-512.
12. S. Mrozowski, *Phys. Rev.*, 1952, **85**, 609.
13. H. Tan, R. Zhou and B. Zhang, *J. Power Sources*, 2021, **506**, 230179.
14. A. C. Ferrari and D. M. Basko, *Nat. Nanotechnol.*, 2013, **8**, 235-246.
15. Z. Li, C. Bommier, Z. S. Chong, Z. Jian, T. W. Surta, X. Wang, Z. Xing, J. C. Neuefeind, W. F. Stickle and M. Dolgos, *Adv. Energy. Mater.*, 2017, **7**, 1602894.
16. Z. Jian, C. Bommier, L. Luo, Z. Li, W. Wang, C. Wang, P. A. Greaney and X. Ji, *Chem. Mater.*, 2017, **29**, 2314-2320.
17. B. Cao, H. Liu, B. Xu, Y. Lei, X. Chen and H. Song, *J. Mater. Chem.A*, 2016, **4**, 6472-6478.
18. M. Ou, Y. Zhang, Y. Zhu, C. Fan, S. Sun, J. Feng, X. Sun, P. Wei, J. Xu and J. Peng, *ACS Appl. Mater. Interfaces*, 2021.
19. D. Zhou, M. Peer, Z. Yang, V. G. Pol, F. D. Key, J. Jorne, H. C. Foley and C. S. Johnson, *J. Mater. Chem.A*, 2016, **4**, 6271-6275.
20. H. Yamamoto, S. Muratsubaki, K. Kubota, M. Fukunishi, H. Watanabe, J. Kim and S. Komaba, *J. Mater. Chem.A*, 2018, **6**, 16844-16848.
21. D. Stevens and J. Dahn, *J. Electrochem. Soc.*, 2000, **147**, 1271.
22. D. Stevens and J. Dahn, *J. Electrochem. Soc.*, 2001, **148**, A803.
23. D. Stevens and J. Dahn, *J. Electrochem. Soc.*, 2000, **147**, 4428.
24. B. Zhang, C. M. Ghimbeu, C. Laberty, C. Vix-Guterl and J. m. Tarascon, *Adv. Energy. Mater.*, 2016, **6**, 1501588.
25. K. Kubota, S. Shimadzu, N. Yabuuchi, S. Tominaka, S. Shiraishi, M. Abreu-Sepulveda, A. Manivannan, K. Gotoh, M. Fukunishi and M. Dahbi, *Chem. Mater.*, 2020, **32**, 2961-2977.
26. H. Kim, J. Hong, G. Yoon, H. Kim, K.-Y. Park, M.-S. Park, W.-S. Yoon and K. Kang, *Energy Environ. Sci.*, 2015, **8**, 2963-2969.
27. N. Sun, Z. Guan, Y. Liu, Y. Cao, Q. Zhu, H. Liu, Z. Wang, P. Zhang and B. Xu, *Adv. Energy. Mater.*, 2019, **9**, 1901351.
28. J. Jagiello and J. P. Olivier, *Carbon*, 2013, **55**, 70-80.
29. J. Jagiello and J. P. Olivier, *Adsor*, 2013, **19**, 777-783.
30. C. Matei Ghimbeu, J. Górká, V. Simone, L. Simonin, S. Martinet and C. Vix-Guterl, *Nano Energy*, 2018, **44**, 327-335.
31. A. Beda, C. Vaultot and C. M. Ghimbeu, *J. Mater. Chem.A*, 2021, **9**, 937-943.
32. J.-B. Kim, G.-H. Lee, V. W.-h. Lau, J. Zhang, F. Zou, M. Chen, L. Zhou, K.-W. Nam and Y.-M. Kang, *J. Phys. Chem. C*, 2021, **125**, 14559-14566.
33. Y. Wen, K. He, Y. Zhu, F. Han, Y. Xu, I. Matsuda, Y. Ishii, J. Cumings and C. Wang, *Nat. Commun*, 2014, **5**, 1-10.
34. Z. Zhu, F. Cheng, Z. Hu, Z. Niu and J. Chen, *J. Power Sources*, 2015, **293**, 626-634.
35. H. Kim, J. Hong, Y. U. Park, J. Kim, I. Hwang and K. Kang, *Adv. Funct. Mater.*, 2015, **25**, 534-541.

36. Z.-L. Xu, G. Yoon, K.-Y. Park, H. Park, O. Tamwattana, S. J. Kim, W. M. Seong and K. Kang, *Nat. Commun.*, 2019, **10**, 1-10.
37. M. Goktas, B. Akduman, P. Huang, A. Balducci and P. Adelhelm, *J. Phys. Chem. C*, 2018, **122**, 26816-26824.
38. Y. Miao, J. Zong and X. Liu, *Mater. Lett.*, 2017, **188**, 355-358.
39. W. Luo, Z. Jian, Z. Xing, W. Wang, C. Bommier, M. M. Lerner and X. Ji, *ACS Cent. Sci.*, 2015, **1**, 516-522.
40. X. Yao, Y. Ke, W. Ren, X. Wang, F. Xiong, W. Yang, M. Qin, Q. Li and L. Mai, *Adv. Energy Mater.*, 2019, **9**, 1803260.
41. S. Alvin, D. Yoon, C. Chandra, H. S. Cahyadi, J.-H. Park, W. Chang, K. Y. Chung and J. Kim, *Carbon*, 2019, **145**, 67-81.
42. J. Ding, H. Wang, Z. Li, A. Kohandehghan, K. Cui, Z. Xu, B. Zahiri, X. Tan, E. M. Lotfabad and B. C. Olsen, *ACS nano*, 2013, **7**, 11004-11015.
43. Z.-E. Yu, Y. Lyu, Y. Wang, S. Xu, H. Cheng, X. Mu, J. Chu, R. Chen, Y. Liu and B. Guo, *Chem. Commun.*, 2020, **56**, 778-781.
44. H. Au, H. Alptekin, A. C. Jensen, E. Olsson, C. A. O'Keefe, T. Smith, M. Crespo-Ribadeneyra, T. F. Headen, C. P. Grey and Q. Cai, *Energy Environ. Sci.*, 2020, **13**, 3469-3479.
45. A. Kamiyama, K. Kubota, D. Igarashi, Y. Youn, Y. Tateyama, H. Ando, K. Gotoh and S. Komaba, *Angew. Chem. Int. Ed.*, 2021, **60**, 5114-5120.
46. C. Guo, K. Zhang, Q. Zhao, L. Pei and J. Chen, *Chem. Commun.*, 2015, **51**, 10244-10247.
47. Y. Ham, V. Ri, J. Kim, Y. Yoon, J. Lee, K. Kang, K.-S. An, C. Kim and S. Jeon, *Nano Res.*, 2021, **14**, 1382-1389.
48. L. Bugnon, C. J. Morton, P. Novak, J. Vetter and P. Nesvadba, *Chem. Mater.*, 2007, **19**, 2910-2914.
49. J.-E. Lim and J.-K. Kim, *Korean J. Chem. Eng.*, 2018, **35**, 2464-2467.
50. X. Liu and Z. Ye, *Adv. Energy Mater.*, 2021, **11**, 2003281.
51. S. Wang, L. Wang, Z. Zhu, Z. Hu, Q. Zhao and J. Chen, *Angew. Chem.*, 2014, **126**, 6002-6006.
52. H.-g. Wang, S. Yuan, Z. Si and X.-b. Zhang, *Energy Environ. Sci.*, 2015, **8**, 3160-3165.
53. A. Tripathi, Y. Chen, H. Padhy, S. Manzhos and P. Balaya, *Energy Technol.*, 2019, **7**, 1801030.
54. H. g. Wang, S. Yuan, D. I. Ma, X. I. Huang, F. I. Meng and X. b. Zhang, *Adv. Energy Mater.*, 2014, **4**, 1301651.
55. L. Zhou, Y. Zhang, S. Amzil, T. Qiu, W. Xu, F. Jiang, Z. Fang, J. Huang and G. Dai, *Appl. Surf. Sci.*, 2021, **542**, 148581.
56. A. Vizintin, J. Bitenc, A. K. Lautar, J. Grdadolnik, A. R. Vitanova and K. Pirnat, *ChemSusChem*, 2020, **13**, 2328.
57. Q. Zhao, W. Zhao, C. Zhang, Y. Wu, Q. Yuan, A. K. Whittaker and X. S. Zhao, *Energy Fuels*, 2020, **34**, 5099-5105.
58. M. Miroshnikov, K. Kato, G. Babu, N. Kumar, K. Mahankali, E. Hohenstein, H. Wang, S. Satapathy, K. P. Divya and H. Asare, *ACS Appl. Energy Mater.*, 2019, **2**, 8596-8604.
59. M. Kolek, F. Otteny, J. Becking, M. Winter, B. Esser and P. Bieker, *Chem. Mater.*, 2018, **30**, 6307-6317.